Journal of Medical Imaging

MedicalImaging.SPIEDigitalLibrary.org

Photoacoustic-based catheter tracking: simulation, phantom, and *in vivo* studies

Alexis Cheng
Younsu Kim
Yuttana Itsarachaiyot
Haichong K. Zhang
Clifford R. Weiss
Russell H. Taylor
Emad M. Boctor

SPIE.

Alexis Cheng, Younsu Kim, Yuttana Itsarachaiyot, Haichong K. Zhang, Clifford R. Weiss, Russell H. Taylor, Emad M. Boctor, "Photoacoustic-based catheter tracking: simulation, phantom, and *in vivo* studies," *J. Med. Imag.* **5**(2), 021223 (2018), doi: 10.1117/1.JMI.5.2.021223.

Photoacoustic-based catheter tracking: simulation, phantom, and *in vivo* studies

Alexis Cheng,[a] Younsu Kim,[a] Yuttana Itsarachaiyot,[b] Haichong K. Zhang,[a] Clifford R. Weiss,[c,d,e] Russell H. Taylor,[a,b,e] and Emad M. Boctor[a,e,f,*]
[a]Johns Hopkins University, Department of Computer Science, Baltimore, Maryland, United States
[b]Johns Hopkins University, Department of Mechanical Engineering, Baltimore, Maryland, United States
[c]Johns Hopkins University, Department of Biomedical Engineering, Baltimore, Maryland, United States
[d]Johns Hopkins University, Department of Surgery, Baltimore, Maryland, United States
[e]Johns Hopkins University, Department of Radiology, Baltimore, Maryland, United States
[f]Johns Hopkins University, Department of Electrical Engineering, Baltimore, Maryland, United States

Abstract. Catheters are commonly used in many procedures and tracking and localizing them is critical to patient safety and surgical success. The standard of care for catheter tracking is with the use of fluoroscopy. Alternatives using conventional tracking technologies such as electromagnetic trackers have been previously explored. This work explores the use of an emerging imaging modality, photoacoustics, as a means for tracking. A piezoelectric (PZT) sensor is placed at the tip of the catheter, allowing it to receive the acoustic signals generated from photoacoustic markers due to the photoacoustic effect. The locations of these photoacoustic markers are determined by a stereo-camera and the received acoustic signals are converted into distances between the PZT element and the photoacoustic markers. The location of the PZT sensor can be uniquely determined following a multilateration process. This work validates this photoacoustic tracking method in phantom, simulation, and *in vivo* scenarios using metrics including reconstruction precision, relative accuracy, estimated accuracy, and leave-out accuracy. Submillimeter tracking results were achieved in phantom experiments. Simulation studies evaluated various physical parameters relating to the photoacoustic source and the PZT sensor. *In vivo* results showed feasibility for the eventual deployment of this technology. [DOI: 10.1117/1.JMI.5.2.021223]

Keywords: catheter tracking; image-guided procedures; interventional tool guidance; photoacoustics.

Paper 17279SSPRR received Sep. 15, 2017; accepted for publication Feb. 7, 2018; published online Mar. 27, 2018.

1 Introduction

Laparoscopic procedures have become common practice as the demands for shorter hospital stays and faster patient recovery times have increased.[1] This has created a need for the tracking of tools and devices, such as catheters, within the patient body. Catheters are used in many applications, such as renal embolization. In this procedure, a catheter is inserted into the body and is guided manually toward the target through the patient's venous system. One complication that may occur is when the catheter is inserted into an incorrect vein due to a lack of real-time guidance.

Catheters are commonly tracked with either some kind of imaging modality such as fluoroscopy or ultrasound (US) or some kind of tracking system, such as electromagnetic (EM) trackers. X-ray fluoroscopy-based systems[2] are the most common, but they have a very obvious disadvantage. X-ray fluoroscopy delivers a radiation dose to the patient for a nontherapeutic purpose and this risk is elevated with young individuals or pregnant women. Due to its harmful nature, its use for catheter tracking is also diminished because it will generally not be used in a real-time and continuous manner. The general use-case scenario is to take intermittent x-ray fluoroscopy images as the catheter is manually inserted. Another drawback with fluoroscopy-based systems is that they only provide tracking in the x-ray image plane unless some multiview fluoroscopic reconstruction is used at the expense of additional radiation. On the other hand, EM-based catheter tracking systems[3] can provide real-time tracking. In these systems, an EM sensor will be placed on the catheter, whereas a field generator is placed external to the patient. As long as the EM sensor is within the field generator's tracking volume, real-time catheter tracking can be achieved. However, EM tracking places certain restrictions on the types of tools that can be used during the procedure, as ferromagnetic materials significantly affect the tracking accuracy. An additional registration solution may be necessary to relate the tracked catheter in the EM frame and the CT/x-ray/fluoroscopy frame.

In this work, we present a catheter tracking technology that makes use of the photoacoustic (PA) effect. Photoacoustic imaging is an emerging imaging modality that captures information about the optical properties of the target material or medium. Its capabilities are based on the photoacoustic effect, which can be described as a conversion from light to acoustic pressure. This acoustic pressure can then be received by a conventional US transducer or a piezoelectric (PZT) element. Therefore, photoacoustic imaging has been mainly used as an imaging modality for interventions, such as prostate brachytherapy.[4,5] Its use as a tracking technology has been fairly limited. We previously demonstrated methods for tracking US transducers using photoacoustic markers, points that can be

*Address all correspondence to: Emad M. Boctor, E-mail: eboctor1@jhmi.edu

2329-4302/2018/$25.00 © 2018 SPIE

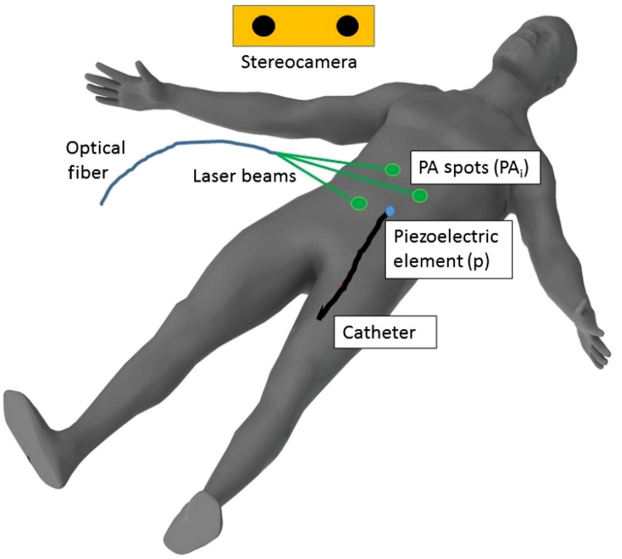

Fig. 1 Photoacoustic catheter tracking concept figure. Multiple photoacoustic spots are projected onto the surface of the patient body, generating an acoustic signal due to the photoacoustic effect. A stereocamera and PZT element can simultaneously capture data related to these spots.

simultaneously observed optically and acoustically.[6] This external US tracking method can theoretically be used in conjunction with this proposed catheter tracking method. A catheter tracking method using photoacoustics would increase the attractiveness of photoacoustic systems by providing them with the means to be an imaging and general tool tracking solution.

Figure 1 shows our concept for photoacoustic catheter tracking. We leverage the use of photoacoustic markers, denoted as PA_i. A stereo camera (SC) is used to observe these markers optically. These markers are nonphysical entities generated on the surface of the medium or on a synthetic surface placed on the medium. A US sensor, a PZT element in our case, is also attached to the catheter tip, denoted as p, and acts as an acoustic sensor. The signal received by the PZT element for each marker will correspond to a distance measure between the marker and the PZT element itself. If there are more than three well-structured photoacoustic markers, the catheter tip's location with respect to the SC system can be computed. This method addresses the limitations described for x-ray fluoroscopy-based and EM-based catheter tracking systems, but it does place a constraint that the SC system must have line of sight to the surface. In addition, if one were to use a synthetic surface with x-ray/optical markers, one can relate the tracked catheter position with respect to preoperative CT or intraoperative fluoroscopy.

2 Technical Approach

This photoacoustic catheter tracking method has four main components: data collection, SC segmentation, US signal segmentation, and PZT element localization.

2.1 *Data Collection*

In our method, there are two sources of data that must be synchronized and collected. The first source is from the SC system. Naturally, the images acquired must by synchronized with the light source used to stimulate PA US emission. In this case, we use the external hardware trigger from the laser system to trigger image capture. This external hardware trigger is also used to trigger PZT signal collection. For the time being, we collect data from a single photoacoustic marker at a time. This keeps the PZT signals independent and not accumulated from multiple photoacoustic markers. Doing so simplifies the segmentation process at the expense of practicality.

2.2 *Stereo-Camera Segmentation*

SC segmentation is the process that takes the images acquired of a single photoacoustic marker and recovers the three-dimensional (3-D) position of this marker within the SC's coordinate system. This requires the point to first be segmented in each camera image. To accomplish this, we use intensity-based and shape-based filters. To further aid this process and avoid false positives, we remove the background in the camera image by subtracting an image that does not contain the signal. We use the process described in our previous work.[6] After this is completed for each of the camera images, the point can be triangulated into a single 3-D point, denoted as PA_i.

2.3 *Piezoelectric Signal Segmentation*

A PZT element receives this time-synchronized acoustic signal. Since the collection of this acoustic signal is synchronized with the laser, the location of the signal in this waveform represents the time between the laser firing event and the acoustic signal reaching the PZT element, denoted as ToF_i. A bandpass filter is used to remove noise in cases, where the acoustic signal may be weak. Following that, we use a peak detector to determine the aforementioned time between the laser firing event and the acoustic signal reaching the PZT. A sample of a collected photoacoustic signal can be shown in Fig. 2.

2.4 *Piezoelectric Element Localization*

The previous components obtained a 3-D position for each photoacoustic marker as well as a measure of time between the PZT element and each of these positions. Assuming that the medium has a homogeneous speed of sound (SoS) each of these measures of time can be converted to distance. This forms a trilateration or multilateration problem. One can then

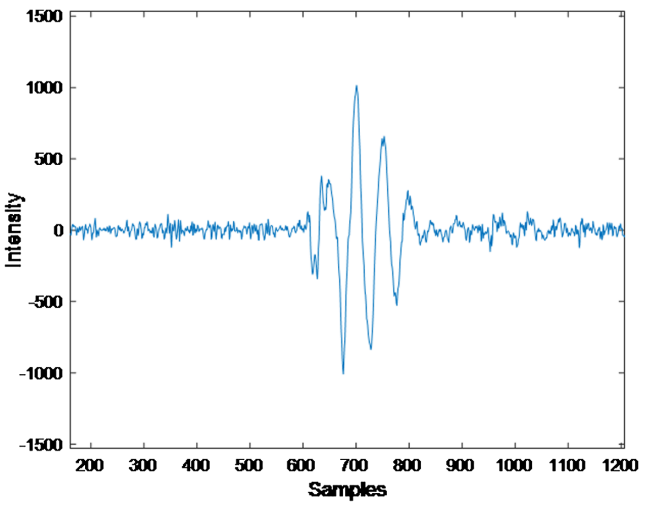

Fig. 2 Sample acoustic signal received by the PZT element.

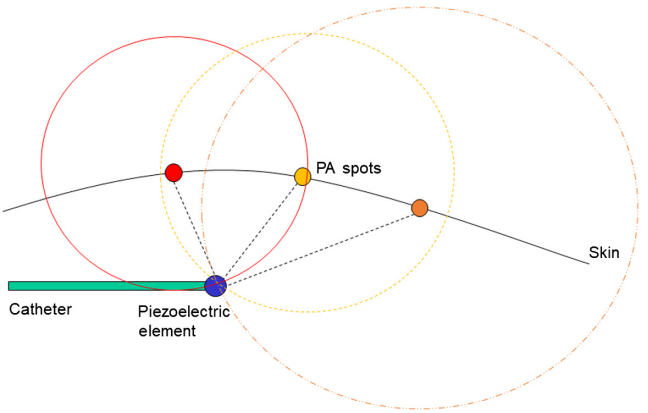

Fig. 3 Graphical description of PZT element localization.

write a distance equation as shown in Eq. (1). With multiple PA spots, this becomes a system of quadratic equations and can be solved when there are at least three noncollinear and well-structured PA spots. In the case of three PA spots, there will be two solutions where the PZT element is either above or below the body surface, with the latter being the desired solution. This ambiguity can be easily solved as the point below the surface will always be farther away from the SC system than the one above the surface. A system with more than three PA spots will require optimization

$$\forall\, i = 1 \ldots n : \underset{p \in R^3}{\operatorname{argmin}} (\|\mathrm{PA}_i - p\|_2 - \mathrm{ToF}_i * \mathrm{SoS})^2. \tag{1}$$

PZT element localization can also be shown graphically in Fig. 3. Each photoacoustic marker is located somewhere in 3-D space. Since the PZT element must lie at a known distance from each of the photoacoustic markers, one can draw a sphere with the distance being its radius, centered about each photoacoustic marker. With three markers, there will be two solutions where each of the three spheres intersects.

The localization methods presented in this section do not attempt to accommodate for errors. We rely on least-squares minimization to reduce the impact of errors. One possible next step is to integrate errors into the localization methods. For example, if we consider the graphical representation shown in Fig. 3, each of these spheres would have a shell with some thickness correlated with the magnitude of the errors. Thus, there could be a set of possible solutions present in the overlapping volume of these spheres. One could envision integrating probabilistic methods to find the most likely solution given some initial knowledge of the error model.

3 Experimental Methods

3.1 *Phantom*

The experiment was performed with a plastisol phantom. The laser system used to generate the photoacoustic markers is Q-switched neodymium-doped yttrium aluminum garnet (Nd:YAG), Brilliant (Quantel Laser, France) laser, operating at 532 nm and ~1 mJ/cm^2. This energy density is well below the safety limits.[7] An SC system consisting of two CMLN-13S2C cameras (Point Grey Research, Canada) is used to acquire the camera images. We used a PZT element as shown in Fig. 4. It is made of a customized PZT5H tube

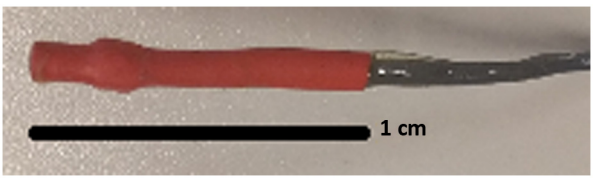

Fig. 4 Example of the PZT element used in these experiments.

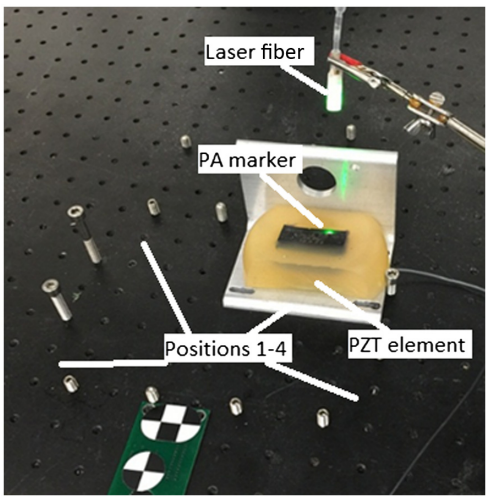

Fig. 5 Experimental setup and apparatus for phantom experiment.

with an outer diameter of 2.08 mm, an inner diameter of 1.47 mm, and a length of 2 mm. The signal from the PZT element is collected using one of the channels of a data acquisition system, the Sonix DAQ (Ultrasonix, Canada), and associated software.[8]

The experiment was designed to test the repeatability of this PZT element localization method. As shown in Fig. 5, the entire setup is placed at four known locations. At each location, 20 photoacoustic markers were collected. Ideally, any three of these photoacoustic markers can be used to localize the same PZT element position. Naturally, there must be some additional constraints on which of these photoacoustic markers are selected, such as noncollinearity and total area. With this data, we were able to analyze a precision metric as well as a relative accuracy metric.

Another experiment was performed on the same apparatus at a single location. A much denser sampling of points was acquired, totaling 65 photoacoustic markers across four linear motions. The data from this experiment can be seen in Fig. 6. The red spots in the left image correspond to the segmentation result. Some rejection was necessary for weak observed signals. From Fig. 6, one can see that the general trend of the observed acoustic signal agrees with our expectation based on the PA spot motion. This experiment was designed to analyze the effects that the number or dimensions of photoacoustic markers has on the proposed method. To validate this, we use a precision metric, a leave-out metric, and an estimated accuracy metric. Each of the metrics for our experiments will be mathematically defined in the following section.

3.2 *Simulation*

Simulations were conducted to examine the effects of four parameters: source radius, sensor radius, sensor length, and

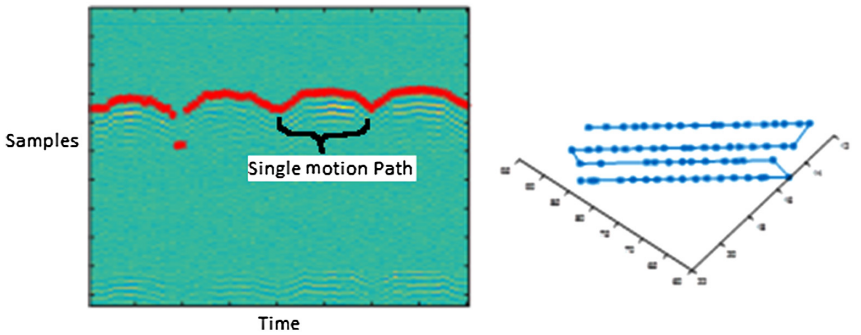

Fig. 6 (a) Observed acoustic signal by the PZT element during PA spot motion annotated with segmentation result and (b) PA spots in the stereocamera space across four linear motions.

SoS. Simulations were done using the k-wave toolbox.[9] Four sources and one sensor were placed in the arrangement as shown in Fig. 7. An accuracy measure comparing the computed location with the known location is used for validation.

3.3 *In Vivo Experiment*

An *in vivo* porcine experiment was performed to evaluate this system in a realistic environment. To enable real-time data collection, the apparatus used was slightly different than in the phantom case. There were two main differences: a galvanometer to actively control the PA spot location and an oscilloscope for PZT sensor data capture. Together, these changes gave us much higher data collection rates than the original phantom experimental setup. This setup can be seen in Fig. 8.

Another key is the use of a photoacoustic active layer, which we put on top of the pig's skin surface as shown in Fig. 9. This gives us control over the generated photoacoustic signal. In addition, we place fiducials on this layer, letting us register our camera tracking system with computed tomography (CT) data for validation purposes. These fiducials also enable surface tracking with the cameras for possible motion compensation due to respiratory activity.

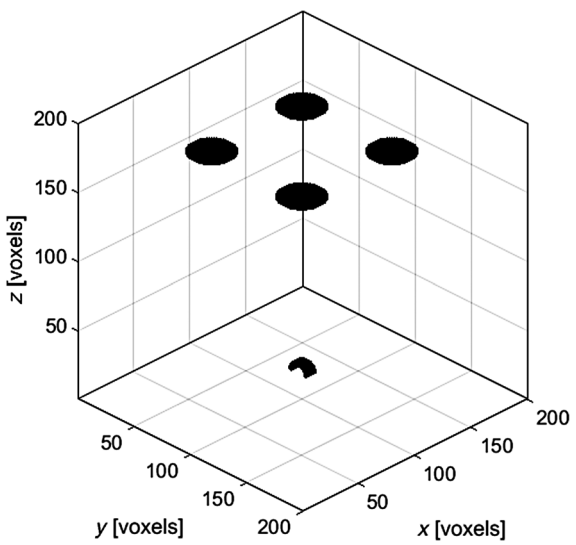

Fig. 7 Arrangement of sources and sensor in simulation environment.

The procedure was as follows: our PZT element tool was placed inside a nine-French catheter. A surgeon then navigated the catheter to a renal vein under the guidance of US and fluoroscopy. Afterward, we use our method to compute the location of the PZT element and compare it with the element segmented from a CT volume.

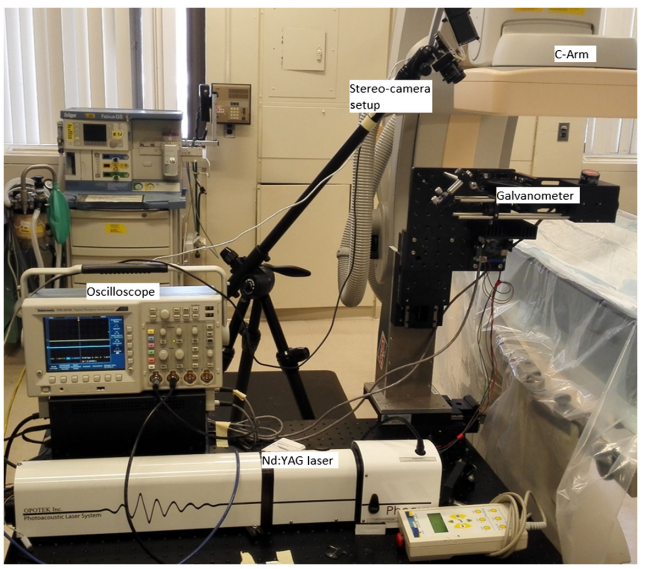

Fig. 8 *In vivo* experimental setup including a laser, a galvanometer, and an oscilloscope.

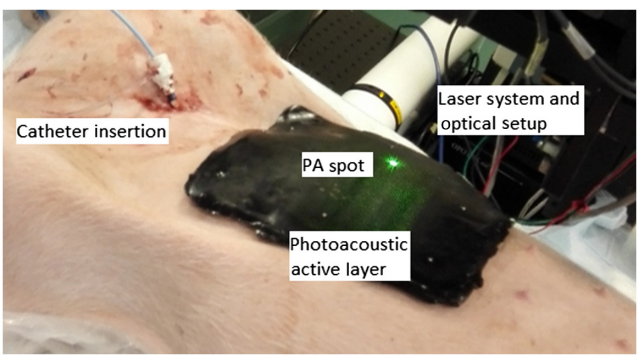

Fig. 9 Photoacoustic active layer placed on top of pig during *in vivo* experiment.

4 Results

4.1 *Phantom*

Several metrics were used to validate our experiments. These include: precision, relative accuracy, leave-out accuracy, and estimated accuracy. For simplicity, we will define several functions used in the metrics. Let PA_i and ToF_i represent a subset of the collected data. Then, our proposed method is a function that uses these two subsets to compute the position of the PZT element, p. This can be written as $p = \mathrm{multilateration}(\mathrm{PA}_i, \mathrm{ToF}_i)$. Each subset of data used will result in a different p being computed, so we can index p as p_j where j corresponds to a single trial. Over a number of trials, a mean, $\bar{p}$, can be computed. Reconstruction precision is defined as shown in Eq. (2). It represents the mean and standard deviation of the computed point to the mean of all computed points

$$\begin{aligned}&\forall\ j = 1 \ldots n\colon \mathrm{distToMean}(j) = \mathrm{norm}(p_j - \bar{p})\\ &\mathrm{RP} = \mathrm{mean}(\mathrm{distToMean}) \pm \mathrm{std}(\mathrm{distToMean}),\end{aligned} \tag{2}$$

Since the PZT element is moved with known motions, one can define a relative accuracy metric. In this case, $\bar{p}$, will require an index, k, for each location. Relative accuracy is defined as shown in Eq. (3). It represents the difference between the distance of the mean computed point at two locations versus the measured distance. The reconstruction precision and relative accuracy for our first experiment can be seen in Tables 1 and 2.

$$\begin{aligned}&\mathrm{calcDist}(k_1, k_2) = \mathrm{norm}(\bar{p}_{k1} - \bar{p}_{k2})\\ &\mathrm{RA}(k_1, k_2) = \frac{\mathrm{abs}[\mathrm{calcDist}(k_1, k_2) - \mathrm{measDist}(k_1, k_2)]}{\mathrm{measDist}(k_1, k_2)}.\end{aligned} \tag{3}$$

Leave-out accuracy uses the observed data that was not used to compute the PZT location as a means for validation. As we mentioned previously, each computed point uses a subset of the collected data. The remaining data can then serve as test points for validation. This metric can be seen in Eq. (4). It takes the computed point for each subset of data and finds its distance to each PA_i not within the subset. This can then be compared directly to the acoustically measured distance, $\mathrm{ToF}_i * \mathrm{SoS}$

$$\begin{aligned}&\forall\ i, j\colon \mathrm{diffDistToTestPoints}(i, j) = \mathrm{abs}(\|\mathrm{PA}_i - p_j\|_2 - \mathrm{ToF}_i * \mathrm{SoS})\\ &\mathrm{LA} = \mathrm{mean}(\mathrm{diffDistToTestPoints}) \pm \mathrm{std}(\mathrm{diffDistToTestPoints}).\end{aligned} \tag{4}$$

Estimated accuracy is a measure to compare the computed PZT location with the estimated ground truth point. Ideally, one would have a ground truth point to directly compare with the computed PZT location. One possible way of obtaining an estimated ground truth point is through the use of an independent imaging modality such as CT. This is what we use for our *in vivo* experiments. However, we use an alternative for our phantom experiments due to difficulties with making the bench setup compatible with the CT imaging system. We use an estimated one instead based on a consensus from all of the data. This consensus, q, is computed using our multilateration method with all of the data as the input. Estimated accuracy is then the difference between each computed PZT location and the consensus, q, and is shown as

$$\begin{aligned}&\forall j\colon \mathrm{distToGroundTruth}(j) = \mathrm{norm}(p_j - q)\\ &\mathrm{EA} = \mathrm{mean}(\mathrm{distToGroundTruth}) \pm \mathrm{std}(\mathrm{distToGroundTruth}).\end{aligned} \tag{5}$$

In addition, we describe a partition and span concept as two parameters to investigate how the size or number of PA spots affects the error metrics. Both concepts are based on dividing the available points into different regions, then selecting a point randomly from each region. The partition parameter refers to the number of divisions each of the motion paths are split up equally into. For example, if the partition parameter is two, then each of the four motion paths are divided in two into a total of eight regions. A single point is randomly chosen from each region, resulting in a total of eight points being used for localization. Partitioning will allow us to see the effects that the number of PA spots has on the error metrics.

Span is a subset of the set of partitioned regions. We fix the number of partitions to a constant and pick a subset of them. The selection of this subset is chosen by the span parameter. An example can be seen in Fig. 10. Each motion path is split up into eight partitions, with them being numbered incrementally from the center of each motion path. The numbered regions matching the span parameter will be the ones, where a single point is randomly selected from each of them. We can see that the span parameter is analyzing the effects of the size of the PA spots, while keeping the number of PA spots fixed. The results for the second experiment analyzing the reconstruction

Table 1 Phantom experiment 1 reconstruction precision.

Location	Reconstruction precision (mm)
Bottom left	1.60 ± 1.13
Top left	1.46 ± 0.94
Bottom right	2.14 ± 1.46
Top right	3.12 ± 2.43

Table 2 Phantom experiment 1 relative accuracy.

Locations	Calculated distance (mm)	Measured distance (mm)	Relative accuracy (%)
LB and LT	69.93	71.12	1.71
RB and RT	68.43	71.12	3.93
LB and RB	96.66	93.47	3.30
LT and RT	96.30	93.47	2.94

4	3	2	1	1	2	3	4
4	3	2	1	1	2	3	4
4	3	2	1	1	2	3	4
4	3	2	1	1	2	3	4

Fig. 10 Sample description of span. The numbers represent the span parameter corresponding to the regions in which a point is selected for catheter localization.

Table 3 Phantom experiment 2 partition analysis using reconstruction precision, leave-out accuracy, and estimated accuracy.

Partition	Reconstruction precision (mm)	Leave-out accuracy (mm)	Estimated accuracy (mm)
2	1.07 ± 0.51	2.38 ± 1.33	1.25 ± 0.74
3	0.82 ± 0.40	2.33 ± 1.32	0.95 ± 0.54
4	0.70 ± 0.35	2.32 ± 1.32	0.81 ± 0.48
5	0.58 ± 0.29	2.28 ± 1.31	0.67 ± 0.40
6	0.45 ± 0.22	2.21 ± 1.30	0.52 ± 0.41

Table 4 Phantom experiment 2 span analysis using reconstruction precision, leave-out accuracy, and estimated accuracy.

Span	Reconstruction precision (mm)	Leave-out accuracy (mm)	Estimated accuracy (mm)
1	0.40 ± 0.15	2.55 ± 1.42	1.06 ± 0.29
2	0.68 ± 0.23	2.06 ± 1.15	1.05 ± 0.29
3	0.75 ± 0.26	2.49 ± 1.35	1.05 ± 0.30
4	1.07 ± 0.60	2.31 ± 1.30	1.05 ± 0.30

precision, the leave-out accuracy, and the estimated accuracy under various partition and span parameter values is found in Tables 3 and 4.

4.2 *Simulation*

The first parameter varied was the source radius. The evolution of this parameter can be seen in Fig. 11. The results can be seen in Table 5. The second parameter varied was the sensor radius. The evolution of this parameter can be seen in Fig. 12. The results can be seen in Table 6. The third parameter varied was the sensor radius. The evolution of this parameter can be seen in Fig. 13. The results can be seen in Table 7. The fourth parameter varied was the assumed SoS. The true SoS is fixed and only the assumed SoS used in the algorithm is varied. The results can be seen in Table 8.

In addition to simulating parameters related to the physical apparatus, we also want to quantify the sensitivity of this localization method to errors or uncertainties in the ToFs or distance measurements between the sensor and each of the PA markers. We simulate the scenario where we have a set of 121 PA sources divided in a 2-cm square. The sensor is then placed at a distance of 9-cm perpendicular to this square. We then add a random error selected from a zero-mean uniform distribution to each of the distances between a PA source and the sensor. We vary the maximum absolute error. The results can be seen in Table 9. We choose the position parameters based on our *in vivo* scenario.

Table 5 Change in accuracy due to change in simulated source radius.

Radius	1 (mm)	2 (mm)	3 (mm)	4 (mm)	5 (mm)
X	0	0.16	0.16	0.16	0
Y	0	0	0	0	0
Z	−0.16	−0.04	0.20	0.44	0.72
Norm	0.16	0.16	0.26	0.47	0.72

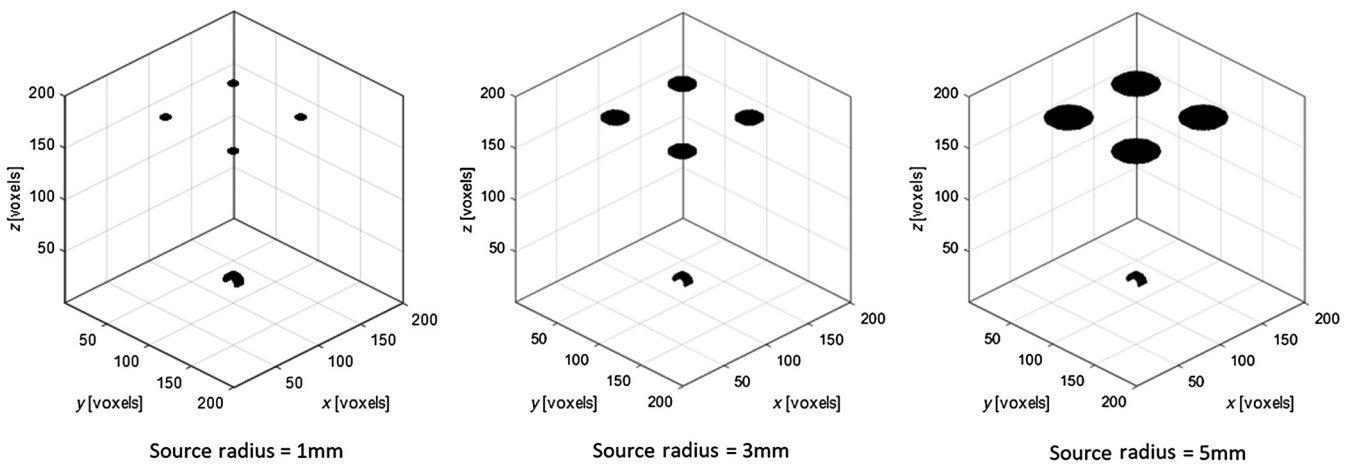

Fig. 11 Evolution of sources and sensor in simulation environment with varying source radius.

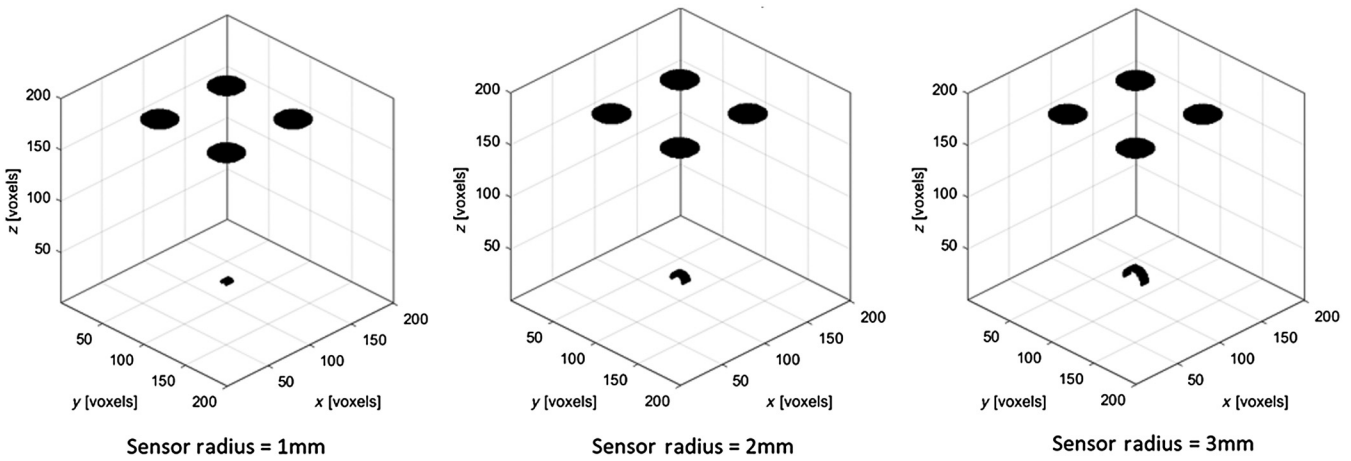

Fig. 12 Evolution of sources and sensor in simulation environment with varying sensor radius.

Table 6 Change in accuracy due to change in simulated sensor radius.

Radius	1 (mm)	1.5 (mm)	2 (mm)	2.5 (mm)	3 (mm)
X	0.16	0.16	0.16	0.16	0
Y	0	0	0	0	0
Z	0.55	0.50	0.44	0.47	0.41
Norm	0.57	0.52	0.47	0.49	0.44

Table 7 Change in accuracy due to change in simulated sensor length.

Radius	1 (mm)	1.5 (mm)	2 (mm)	2.5 (mm)	3 (mm)
X	0	0	0.16	0.16	0.16
Y	0	0	0	0	0
Z	0.48	0.48	0.44	0.44	0.44
Norm	0.48	0.48	0.47	0.47	0.47

4.3 *In Vivo Experiment*

Figure 14 shows a possible visualization result when using this method. A distance map is created on the surface, with the aim to give the surgeon some two-dimensional information about where the catheter tip may be relative to the surface. The three other windows show the real-time segmentation results during data collection.

Figure 15 shows three perpendicular slices of a CT volume corresponding to our computed PZT element position. Each of the colored lines represents the three slices (saggital, axial, and

Table 8 Change in accuracy due to change in simulated SoS.

SoS	1460 (m/s)	1480 (m/s)	1500[a] (m/s)	1520 (m/s)	1540 (m/s)
X	0.1	0.2	0.16	0.16	0.17
Y	0	0	0	0	0
Z	1.6	1.0	0.44	−0.13	0.67
Norm	1.6	1.0	0.47	0.21	0.71

[a]True SoS.

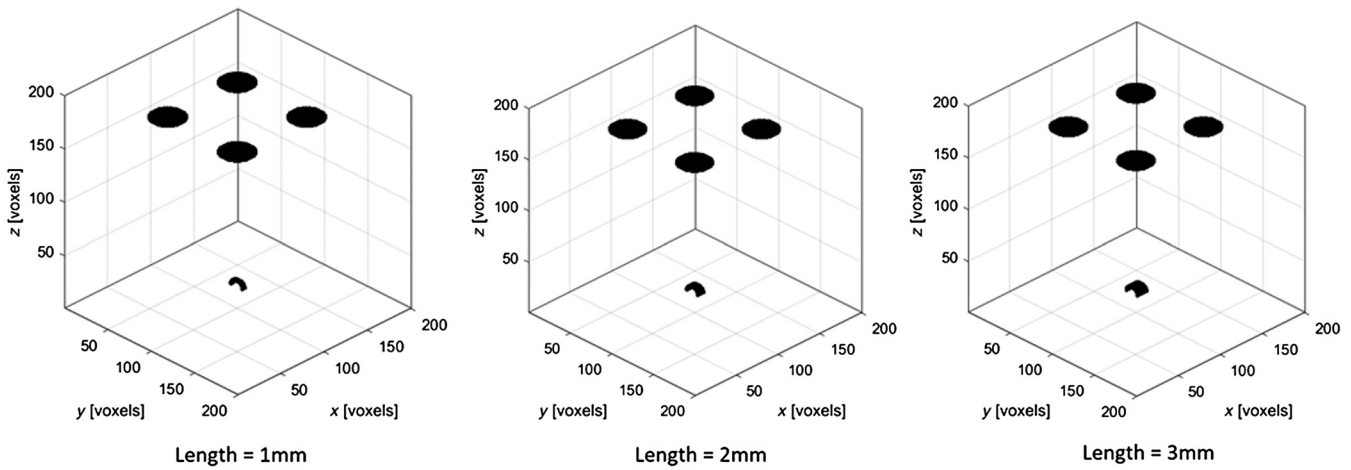

Fig. 13 Evolution of sources and sensor in simulation environment with varying sensor length.

Table 9 Simulation studying sensitivity of the localization result to errors in the source-sensor distance.

Maximum absolute error (mm)	2 (mm)	4 (mm)	6 (mm)	8 (mm)	10 (mm)
Minimum	0.46	0.41	0.26	0.31	0.31
Mean	1.59	2.75	4.01	5.25	6.61
Median	1.47	2.56	3.72	4.89	6.16
Maximum	6.13	10.10	14.18	19.88	24.64
STD	0.67	1.34	2.04	2.71	3.43

coronal). Subjectively, it can be seen that the detected position is close to the position in the CT volume.

Across 10,000 trials of using different subsets of 100 PA markers, the resulting metrics can be seen in Table 10.

5 Discussion

From the results of the first experiment seen in Tables 1 and 2, we can see that the PZT element localization results are fairly repeatable and comparable to conventional tracking-based systems. There are several sources of error that contributed to these results. First, SC errors are tied to how well calibrated the system is and can fluctuate depending on the specific SC system used. Second, segmentation errors of the photoacoustic markers and acoustic signal will propagate to the final localization result. These errors are also magnified since the photoacoustic markers themselves are only several centimeters apart. Third, if the

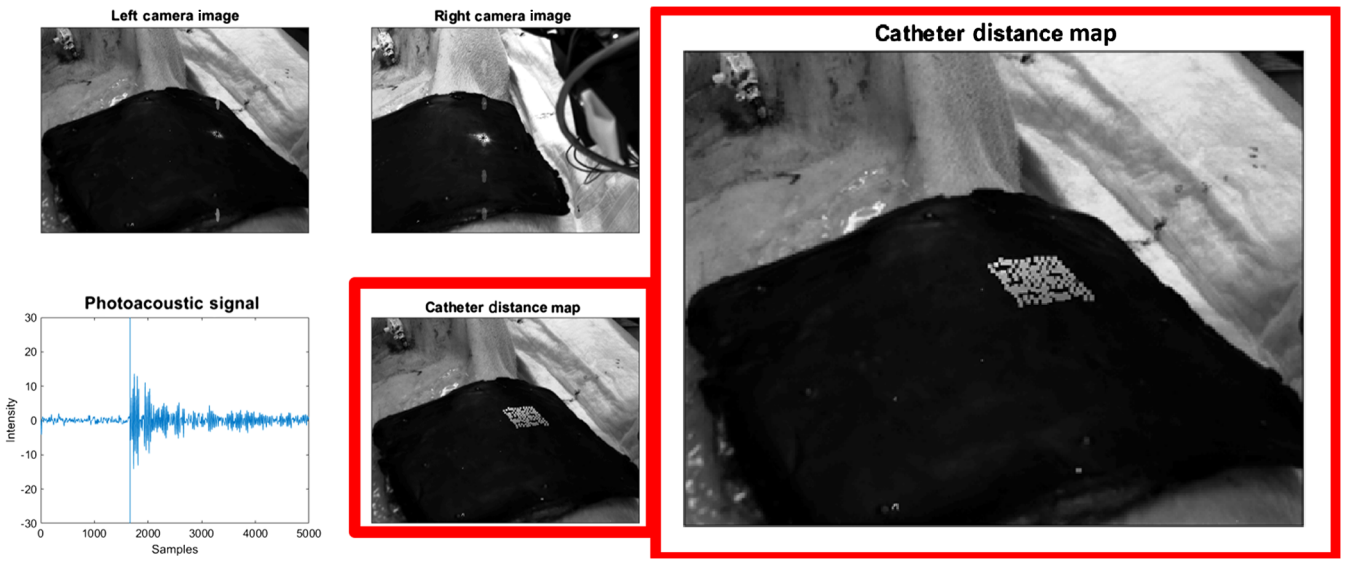

Fig. 14 Software result during *in vivo* experiment and possible visualization of a surface distance map.

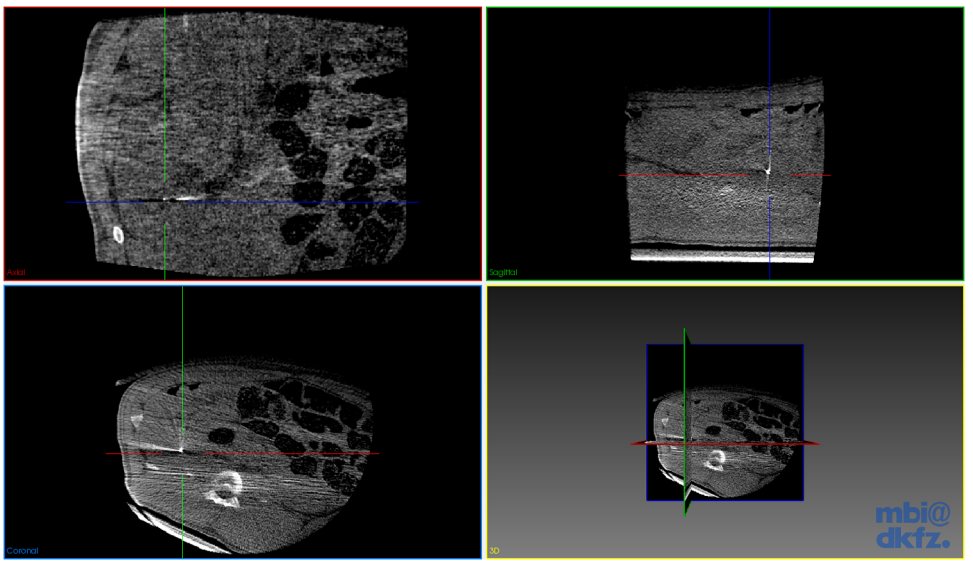

Fig. 15 Perpendicular slices of a CT volume at the computed PZT element position during *in vivo* experiment.

Table 10 *In vivo* experimental results using reconstruction precision, estimated accuracy, and leave-out accuracy.

Metric	RP (mm)	EA (mm)	LA (mm)
Minimum	0.05	1.73	0
Mean	2.59	8.69	1.26
Median	1.92	8.20	0.79
Maximum	12.33	18.88	18.89
STD	1.83	2.60	1.91

photoacoustic markers are very close to each other, the quadratic system becomes less well defined. Ideally, the markers would be spaced far apart, but there are drawbacks to doing so. The received acoustic signal by the PZT element decreases in amplitude as the marker moves further away on the surface of the medium. It may become necessary to increase the energy density of the laser to counteract this effect.

Table 3 shows the expected trend for each of the metrics used. As the partition parameter increases, the number of points used for multilateration increases. This seems to result in an improvement in each of the metrics as each of the metrics decrease in magnitude as the partition parameter increases. However, we see that the decrease is marginal for the leave-out accuracy metric. This may indicate that there remains some segmentation noise in either or both of the stereocamera points or the PZT element signal.

Interestingly, Table 4 does not show the expected trend. The only metric that shows a trend is the reconstruction precision. In this case, it is increasing as the span parameter increases. One explanation for this may be that PA spots that are closer together end up resulting in a computed spot that is more consistent. We expected the metrics to improve as the span parameter increased as multilateration theoretically operates better when the PA spots are further apart. This result may again be an indication that segmentation errors eroded any effects that an increased span parameter may have had on the method.

There are a few observations to make from the simulation results. As expected, we can see from Table 5 that the source radius has a detrimental effect on the localization result. In a sense, this causes the sources to act less, such as a point target, which was one of our assumptions. On the other hand, the sensor radius and sensor length have minimal effect on the resulting accuracy, as can be seen in Tables 6 and 7. This may be because we apply correction to the time of flights based on our knowledge about the sensor. For example, if the sensor is 2 mm in radius, 2 mm is added to each of the time of flights/distances. The simulated varying SoS results shown in Table 8 slightly differ from expectations in that the minimum error is not at the true SoS. We believe that this is due to the partial volume effects within the simulation itself as both the source and sensor surfaces have a finite thickness associated with them. The sensitivity results shown in Table 9 seem to indicate that this method is fairly sensitive to the maximum absolute error on the source-sensor distances as a centimeter of error can lead to an accuracy of 6 to 7 mm on average.

The *in vivo* experiments and results presented in Table 10 show that this method is feasible in an *in vivo* setting. While the errors are higher than the phantom experiments, they may still be useful depending on the surgical procedure. If we consider the sensitivity results in Table 9, there may be source-sensor uncertainties of a centimeter. In addition, there are also error sources due to registration with the ground truth CT modality. Another likely source of error is tissue inhomogeneity and consequent SoS inhomogeneity. In our models, we assume a single SoS value for the ToF measurements from each PA marker. This is unlikely to be the case in a realistic setting because each acoustic path may differ in terms of its tissue composition. While it is impossible to solve for a unique SoS for each acoustic path, one possible future direction may be to allow for some differences in SoS for each acoustic path constrained by their relative positions to each other. Another possibility is to use preoperative imaging as a means for estimating SoS. Certain data processing steps such as surface or SoS compensation, as well as improvements to the apparatus, such as reducing the source radius, may reduce these errors.

Earlier, we mentioned that we sequentially collect data, one point at a time. While this is possible in a bench experiment, it is impossible in practice while the catheter is moving. The main challenge in concurrently collecting data from multiple photoacoustic markers is distinguishing the acoustic signals in the received PZT waveform. Currently, this method requires known correspondence between the photoacoustic marker positions and its distance measure. Another direction is modeling for inhomogeneous SoS within the body. Further development would be necessary to improve the practicality of this method.

This localization method can have a synergistic effect on current fluoroscopic catheter tracking surgical workflows. The results shown here represent a first step toward reducing the need for continuous fluoroscopy during catheter insertion. However, before this system can be used in practice, several improvements and developments are necessary. The apparatus is currently too bulky to be used in conjunction with x-ray fluoroscopy. Reducing the size of the laser or making the light delivery system hand-held would be a necessary development. Additionally, the current data acquisition rate limits this method as a static tracking method. Improving the acquisition rate may be possible with the use of more sophisticated light delivery methods such as coded excitation. Increasing the tracking range by integrating a robotic light delivery manipulation component would also improve the practicality of this system.

6 Conclusion

We experimentally demonstrated the localization of a single PZT element. The proposed system can be used to track catheters and provides photoacoustic surgical systems with an additional function. The resulting localization precision and relative accuracy are comparable with existing tracking methods. In addition, we showed a reconstruction precision up to 0.4 mm and an estimated accuracy up to 0.5 mm in phantom experiments. We also presented a simulation studying the effects of the source radius, the sensor radius, the sensor length, and the SoS. Promising *in vivo* results were also shown. Future work will the development of concurrent photoacoustic marker projection and its associated methods.

Disclosures

No conflicts of interest, financial or otherwise, are declared by the authors.

Acknowledgments

Financial support was provided primarily by NSF Grant No. IIS-1653322: Co-Robotic Ultrasound Sensing in Bioengineering, and by NIGMS-/NIBIB-NIH Grant No. 1R01EB021396: Slicer+PLUS: Point-of-Care Ultrasound. The authors thank Dr. Jenanan Vairavamurthy and Dr. Tsai Meng for their help during the *in vivo* experiments.

References

1. F. Froghi et al., "Single-incision laparoscopic surgery (SILS) in general surgery: a review of current practice," *Surg. Laparosc. Endosc. Percutan. Tech.* **20**(4), 191–204 (2010).
2. Y. Ma et al., "Real-time x-ray fluoroscopy-based catheter detection and tracking for cardiac electrophysiology interventions," *Med. Phys.* **40**(7), 071902 (2013).
3. B. J. Wood et al., "Navigation with electromagnetic tracking for interventional radiology procedures: a feasibility study," *J. Vasc. Interv. Radiol.* **16**(4), 493–505 (2005).
4. M. A. L. Bell et al., "In vivo visualization of prostate brachytherapy seeds with photoacoustic imaging," *J. Biomed. Opt.* **19**(12), 126011 (2014).
5. M. Xu and L. V. Wang, "Photoacoustic imaging in biomedicine," *Rev. Sci. Instrum.* **77**, 041101 (2006).
6. A. Cheng et al., "Direct three-dimensional ultrasound-to-video registration using photoacoustic markers," *J. Biomed. Opt.* **18**(6), 066013 (2013).
7. International Electrotechnical Commission, "Safety of laser products—part 1: equipment classification and requirements," IEC 60825-1:1993+A1:1997+A2:2001, International Electrotechnical Commission, Geneva (2001).
8. H. J. Kang et al., "Software framework of a real-time pre-beamformed RF data acquisition of an ultrasound research scanner," *Proc. SPIE* **8320**, 83201F (2012).
9. B. Treeby and B. Cox, "k-Wave: MATLAB toolbox for the simulation and reconstruction of photoacoustic wave-fields," *J. Biomed. Opt.* **15**(2), 021314 (2010).

Alexis Cheng received his bachelor's degree in applied science from the University of British Columbia. Currently, he is a PhD student in the Department of Computer Science at Johns Hopkins University. His research interests include ultrasound-guided interventions, photoacoustic tracking, and surgical robotics.

Younsu Kim is a PhD student in the Department of Computer Science at Johns Hopkins University. Prior to joining the PhD program at Johns Hopkins, he worked as a research engineer at Department of Advanced Technology in LG Electronics Inc., Republic of Korea. He received his BE degree in microelectrical engineering from Tsinghua University, Beijing, China, in 2008, and he earned a master's degree in the Department of Electrical and Computer Engineering at Johns Hopkins University, Baltimore, USA, in 2009. His research interests include ultrasound thermal monitoring and ultrasound guided tracking technologies for interventions.

Haichong K. Zhang is a postdoctoral fellow in the Laboratory of Computational Sensing and Robotics at Johns Hopkins University. He received his BS and MS degrees in Human Health Sciences from Kyoto University, Japan, in 2011 and 2013, respectively. After completing his master's degree, he joined the Medical Ultrasound Imaging and Intervention Collaboration (MUSiiC) Laboratory at Johns Hopkins University, and he received his MS and PhD in computer science in 2015 and 2017, respectively. His research interests include advanced robotic instrumentation and imaging with emphasis on ultrasound and photoacoustics for biomedical applications. He has authored more than 40 refereed scientific publications including journals and conference proceedings, and five pending/issued patents.

Russell H. Taylor received his PhD in computer science from Stanford in 1976. After spending 1976 to 1995 as a research staff member and research manager at IBM Research, he moved to Johns Hopkins University, where he is the John C. Malone professor of Computer Science and Director of the Laboratory for Computational Sensing and Robotics. He is the author of over 445 peer-reviewed publications and 59 patents and has received numerous awards and honors.

Emad M. Boctor joined the Russell H. Morgan Department of Radiology and Radiological Science at Johns Hopkins Medical Institute in 2007. His research focuses on image-guided therapy, advanced interventional ultrasound imaging and surgery. He is an Engineering Research Center investigator and holds a primary appointment as an assistant professor in the Department of Radiology and a secondary appointment in both the Computer Science and Electrical Engineering Departments at Johns Hopkins.

Biographies for the other authors are not available.